Flows in Straws: Viscous Flows in One-Dimensional Metamaterial

Peter Breitman, Michael Pukshansky, Anna Zigelman, Ezra Ben Abu, Ofek Peretz, Sefi Givli,
and Amir D. Gat[*]

Faculty of Mechanical Engineering, Technion—Israel Institute of Technology, Haifa 32000, Israel

We propose to incorporate fluids within multistable metamaterials to tailor a desired dynamic response, dictate the magnitude of rate-dependent dissipation, control the sequence and pattern of phase transition, and more. As a simple example we focus on straws, which are commonly used to transfer fluids and are constructed from a one-dimensional (1D) lattice of bistable elements. We first solve for the dynamics of a single element in the unstable spinodal state, reducing or increasing the pressure locally. Using a long-wave approximation, we then model viscous flow and solid phase change within a 1D lattice of bistable frusta. The model is compared with experiments, showing excellent agreement.

I. INTRODUCTION

This study addresses a disconnect between the vision of developing tunable superelastic metamaterials for applications such as configurable materials, vibration mitigation, shock attenuation, and soft robotics, and their present realization. So far, existing studies of multistable metamaterials, which can be thought of as a manifestation of architected superelastic materials due to their inherent ability to provide large reversible deformations and structural programmability, have focused on tailoring the structural properties of the unit cells to obtain desired multistable behavior. Nevertheless, devising a way to enable tunable rate-related properties of the unit cells has not been considered. In this paper, we examine introducing viscous flows within interconnected multistable building blocks for this purpose.

Engineering-design methodology has traditionally avoided structural instabilities in order to prevent catastrophic damage. However, recent advances in the field of architected materials have shown that, by proper design, structural instabilities can be harnessed to devise multistable metamaterials. This relatively new class of mechanical metamaterials has promising potential, especially in applications that require large deformations combined with structural memory, such as foldable structures, reconfigurable materials, energy absorbers, and soft robots [1–11]. Similar to how *standard* mechanical metamaterials enable enhanced mechanical properties, such as negative Poisson ratio and high stiffness-to-mass ratio [12–14], multistable metamaterials are the manifestation of architected superelastic materials and smart materials. There, each unit cell is programmed to undergo specific large distortions when certain conditions are met, a notion that led to the vision that "the material is the machine" [15].

Previous studies of multistable metamaterials have focused mainly on tailoring the *elastic* response of the unit cell to obtain desired multistable properties. In this work, we present the concept of including internal viscous fluid within multistable metamaterials, allowing for tunable rate-dependent properties, nonlocal interaction between unit cells, and sequenced activation. Together with the structural memory and large programmable deformations inherent in multistable metamaterials, the above-mentioned features open the door to exciting applications and development of new materials. By analogy to superelastic or smart materials, one may think of this concept as enabling a tunable kinetic relation [16,17], which dictates the propagation dynamics of phase boundaries in such materials. The ability to tailor both the multistable elastic behavior and the kinetic relation paves the way to extraordinary dynamic behaviors that extend beyond that of natural superelastic and smart materials. This way, for example, vibration mitigation and shock absorption capabilities of multistable metamaterials [18–22] can be significantly enhanced by tuning their internal dissipation.

Incorporating viscous flows in superelastic metamaterials must rely on an adequate understanding of their influence on the overall behavior, and in particular on the propagation of transition fronts. To this end, we use drinking straws as a simple case study prototypical of the more general problem of viscous flows inside multistable metamaterials. We model and experimentally test the dynamics of a viscous flow within "strawlike" structures, for which the viscous resistance is a function of the state of the elements, and study the influence of the internal flow on the overall response and in particular on the propagation of phase-transition fronts. Drinking straws (or strawlike

---

*amirgat@technion.ac.il

structures) are natural candidates for such study since they are multistable objects commonly used for transferring fluids. Despite being an everyday object, the drinking straw features an intriguing mechanical behavior that stems from a unique structure, namely a tandem array of bistable frusta (conical springs) that give rise to multistability. This one-dimensional (1D) multistable structure can be used to construct complex 2D and 3D structures by means of arrays (or lattices) in which the 1D strawlike structure is the basic building block (e.g., [5,23]). Such structures have been shown to enable a wealth of 2D (or 3D) spatial deformation patterns that involve large reversible deformations, e.g., [23]. Previous research on the mechanical properties of straws has mainly focused on equilibrium configurations [24,25]. Compared to the large body of research that deals with viscous flows within "standard" elastic structures (e.g., [26–41]), the interaction between viscous flows and multistable structures has received much less attention [10,42–47]. Recently, a paper by Ilssar *et al.* [48] studied the dynamics of a liquid-filled straw structure including inertial and gravitational forces, although the influence of viscous forces was neglected.

II. PROBLEM DEFINITION AND GOVERNING EQUATIONS

Let us consider a multistable metamaterial, which is a long cylindrical straw composed of many frusta connected in series with a propagating viscous flow inside, as shown in Figs. 1(a) and 1(b). The configuration is axisymmetric and thus we use a radial coordinate system (x, r). Fluid velocity and pressure are (u_x, u_r) and p, respectively. Both fluid viscosity, μ, and density, ρ, are assumed to be constant. We denote the minimal inner radius of the straw (inner region excluding the frusta) by r_c.

We focus on the limit of viscous flow, and thus on the small reduced Reynolds number $Re_r \ll 1$. Following standard lubrication analysis, and neglecting variations in radius due to the frusta, leads to $p = p(x)$ and

$$\frac{r_c^2}{8\mu}\frac{\partial^2 p}{\partial x^2} = \frac{\partial u_b}{\partial x}, \tag{1}$$

where u_b is the speed of the walls in the x-direction. See Appendix A for details of this derivation. Equation (1) governs the flow dynamics. Although Eq. (1) seems quite simple, the problem is complicated due to the relation between u_b and the traction that the fluid applies on the solid, as will be explained below.

The fluidic dynamics is coupled to the elastic properties of the 1D frusta lattice. As an approximation for the relationship between the length of a single bistable element and the tension, which was proposed by Almen and Laszlo [49], we use the trilinear model. According to this common and useful model [50–55], the energy function

may be approximated by three quadratic functions that lead to a piecewise linear pressure-volume relationship, when considering the tension and length of the element. Further discussion regarding this approximation is available in [10].

In our case, the trilinear curve is defined by the stiffnesses, k_{closed} and k_{open}, as well as the stability threshold points $(l_{\text{open}}^{\text{snap}}, f_{\text{open}}^{\text{snap}})$ and $(l_{\text{close}}^{\text{snap}}, f_{\text{close}}^{\text{snap}})$ [see definitions in Fig. 1(c)]. These yield the relation

$$f_e = \begin{cases} k_{\text{closed}}\,(l_i - l^c) \\ f_{\text{open}}^{\text{snap}} + k_s\,(l_i - l_{\text{open}}^{\text{snap}}) \\ k_{\text{open}}\,(l_i - l^o) \end{cases}, \quad \begin{matrix} l_i < l_{\text{open}}^{\text{snap}} \\ l_{\text{open}}^{\text{snap}} < l_i < l_{\text{close}}^{\text{snap}} \\ l_{\text{open}}^{\text{snap}} < l_i, \end{matrix} \tag{2}$$

where l_i is the length of the ith element, and the following relations apply:

$$k_{\text{closed}} = \frac{f_{\text{open}}^{\text{snap}}}{l_{\text{open}}^{\text{snap}} - l^c}, \quad k_s = \frac{f_{\text{close}}^{\text{snap}} - f_{\text{open}}^{\text{snap}}}{l_{\text{close}}^{\text{snap}} - l_{\text{open}}^{\text{snap}}},$$

$$k_{\text{open}} = -\frac{f_{\text{close}}^{\text{snap}}}{l^o - l_{\text{close}}^{\text{snap}}}.$$

The length of the bistable elements at the different states, at rest ($f_e = 0$), is l^c for the closed state (phase I) and l^o for the open state (phase II). The possible force range for bistable elements in phase I is $f_e < f_{\text{open}}^{\text{snap}}$, in the spinodal region $f_{\text{close}}^{\text{snap}} < f_e < f_{\text{open}}^{\text{snap}}$, and in phase II $f_e > f_{\text{close}}^{\text{snap}}$. These coefficients are commonly evaluated by fitting to an experiment [56–58].

In order to relate the tension acting on the bistable elements to the pressure in the fluid, we use a control volume force balance in the x-direction. This yields

$$\pi r_c^2 p(x) - f_e(x) = \pi r_c^2 N p(x_{\text{end}}) - f_{\text{ext}}, \tag{3}$$

relating the pressure within a given location along the channel, $p(x)$, and the total elastic tension in the x-direction, f_e, to the pressure at the outlet of the straw $p(x_{\text{end}})$, and any external force acting on the end of the straw f_{ext}. Moreover, we denote by N, $N \in \{0, 1\}$, the boundary condition at the outlet of the straw, so that for a closed straw $N = 0$, while for an open straw $N = 1$.

Finally, the wall velocity, u_b, at the locations where the bistable elements are connected can be related to the time derivative of the sum of the length of all prior frusta. Between these discrete locations we approximate the velocity in each bistable element as linearly increasing, thus yielding for $\sum_{m=1}^{i-1} l_m < x < \sum_{m=1}^{i} l_m$ that

$$u_b(x, t) = \sum_{m=1}^{i-1}\frac{\partial l_m}{\partial t} + \left(x - \sum_{m=1}^{i-1} l_m\right)\frac{1}{l_i}\frac{\partial l_i}{\partial t}. \tag{4}$$
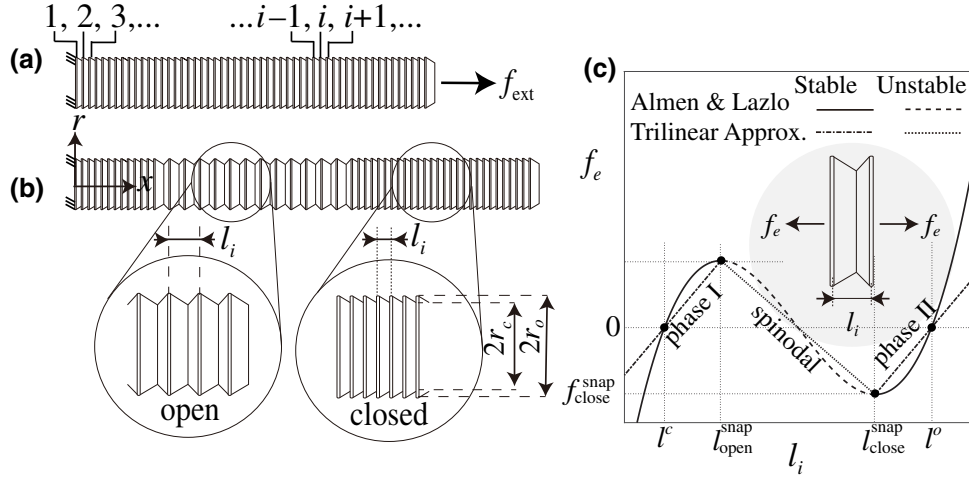
FIG. 1. (a) Illustration of a fluid-filled tube composed of a 1D lattice of closed bistable unit cells. (b) Closeup of both open and closed unit cells, as well as the geometric parameters of each state. (c) Element length l_i to tension force f_e model of Almen and Laszlo [49] (smooth and dashed lines), as well as the trilinear approximation (dotted and dash-dotted lines).

III. RESULTS

To render the problem dimensionless, we define the normalized pressure $P = p/p_c$, flow velocity $U = u/u_c$, wall speed $U_b = u_b/u_c$, element length $L_i = l_i/l_c$, coordinates $(X, R) = (x/x_c, r/r_c)$, snap open force $F_{\text{open}}^{\text{snap}} = f_{\text{open}}^{\text{snap}}/p_c\pi r_c^2$ (and similar scaling for $f_{\text{close}}^{\text{snap}}$), stiffness $K_{\text{closed}} = k_{\text{closed}}l_c/(p_c\pi r_c^2)$ (and similar scaling for k_{open} and k_s), and time $T = tu_c/x_c$ (capital letters denote normalized parameters and the c subscript denotes characteristic values), where characteristic velocity was chosen to be $u_c = p_c r_c^2/\mu x_c$.

The ratio between the length of a single element and the characteristic length of the tube is given by $\varepsilon = l_c/x_c \ll 1$. Transforming Eq. (1) into dimensionless variables and integrating yields the volumetric flux, which is a function of time only (see Appendix A):

$$Q(T) = \pi U_b(X, T) - \frac{\pi}{8}\frac{\partial P}{\partial X}. \quad (5)$$

A. Derivation of the continuous (long-wave) approximation

Let us start by rewriting the wall velocity, u_b, given in Eq. (4), in dimensionless form. Thus, for $\varepsilon \sum_{m=1}^{i-1} L_m < X < \varepsilon \sum_{m=1}^{i} L_m$, we get that

$$U_b(X, T) = \left(X - \varepsilon \sum_{m=1}^{i-1} L_m\right) \frac{1}{L_i}\frac{\partial L_i}{\partial T} + \varepsilon \sum_{m=1}^{i-1} \frac{\partial L_m}{\partial T}. \quad (6)$$

Substituting Eq. (6) into Eq. (5), which we integrate over a single bistable element, yields, for $X \in (\varepsilon \sum_{m=1}^{i-1} L_m, \varepsilon \sum_{m=1}^{i} L_m)$, the following expression

for the pressure P:

$$P = \int_{X=\varepsilon \sum_{m=1}^{i-1} L_m}^{X} \left[8U_b(\tilde{X}, T) - \frac{8}{\pi}Q(T)\right] d\tilde{X}$$
$$+ P|_{X=\varepsilon \sum_{m=1}^{i-1} L_m}$$
$$= P|_{X=\varepsilon \sum_{m=1}^{i-1} L_m} + 4\left(X - \varepsilon \sum_{m=1}^{i-1} L_m\right)$$
$$\times \left[\frac{X - \varepsilon \sum_{m=1}^{i-1} L_m}{L_i}\frac{\partial L_i}{\partial T} + 2\varepsilon \sum_{m=1}^{i-1} \frac{\partial L_m}{\partial T} - \frac{2Q(T)}{\pi}\right].$$
$$(7)$$

Setting $X = \varepsilon \sum_{m=1}^{i} L_m$ to be the end of element i, we obtain a relation between the pressure at the end of element i and the end of element $i - 1$:

$$P|_{X=\varepsilon \sum_{m=1}^{i} L_m} = 4\varepsilon L_i\left[\varepsilon \frac{\partial L_i}{\partial T} + 2\varepsilon \sum_{m=1}^{i-1} \frac{\partial L_m}{\partial T} - \frac{2Q(T)}{\pi}\right]$$
$$+ P|_{X=\varepsilon \sum_{m=1}^{i-1} L_m}.$$
$$(8)$$

Note that Eq. (8) remains valid if we increase all indexes by one, $i \to i + 1$, thus describing the following bistable element. Subtracting Eq. (8) from the equation for the following element, we eliminate the sum term over L_m and

obtain

$$\frac{1}{L_{i+1}}P|_{X=\varepsilon\sum_{m=1}^{i+1}L_m}$$

$$-\left(\frac{1}{L_{i+1}}+\frac{1}{L_i}\right)P|_{X=\varepsilon\sum_{m=1}^{i}L_m}+\frac{1}{L_i}P|_{X=\varepsilon\sum_{m=1}^{i-1}L_m}$$

$$=4\varepsilon^2\left(\frac{\partial L_i}{\partial T}+\frac{\partial L_{i+1}}{\partial T}\right). \tag{9}$$

We can now apply a long-wave approximation and substitute a Taylor series expansion for both P up through order $O(\varepsilon^4)$ and L up through order $O(\varepsilon^2)$, around $X=\varepsilon\sum_{m=1}^{i}L_m$. The difference in the expansion order of P and L is because ε^2 multiplies linear terms involving the derivatives of L on the right-hand side of Eq. (9), whereas the left-hand side of Eq. (9) is free of ε. These series are given by

$$P|_{X=\varepsilon\sum_{m=1}^{i-1}L_m}=P-\varepsilon L_i\frac{\partial P}{\partial X}+\frac{\varepsilon^2 L_i^2}{2}\frac{\partial^2 P}{\partial X^2}$$

$$-\frac{\varepsilon^3 L_i^3}{6}\frac{\partial^3 P}{\partial X^3}+O(\varepsilon^4),$$

$$P|_{X=\varepsilon\sum_{m=1}^{i}L_m}=P,$$

$$P|_{X=\varepsilon\sum_{m=1}^{i+1}L_m}=P+\varepsilon L_{i+1}\frac{\partial P}{\partial X}+\frac{\varepsilon^2 L_{i+1}^2}{2}\frac{\partial^2 P}{\partial X^2}$$

$$+\frac{\varepsilon^3 L_{i+1}^3}{6}\frac{\partial^3 P}{\partial X^3}+O(\varepsilon^4), \tag{10a}$$

and

$$L_i=L(X,T),$$

$$L_{i+1}=L(X,T)+\varepsilon L_{i+1}\frac{\partial L}{\partial X}+O(\varepsilon^2). \tag{10b}$$

Note that the relation between L and L_{i+1} is a power series in L. Substituting Eqs. (10) into Eq. (9), noting that the terms of order $O(1)$ and $O(\varepsilon)$ cancel, and dividing the resultant equation by ε^2, we obtain the following long-wave approximation:

$$\frac{16}{L}\frac{\partial L}{\partial T}=\frac{\partial^2 P}{\partial X^2}$$

$$+\varepsilon\left[2L\frac{\partial^3 P}{\partial X^3}-8\frac{\partial^2 L}{\partial X\partial T}-8\frac{\partial L}{\partial X}\frac{\partial L}{\partial T}+\frac{\partial^2 P}{\partial X^2}\frac{\partial L}{\partial X}\right]$$

$$+O(\varepsilon^2). \tag{11a}$$

This equation is accompanied by the scaled version of Eqs. (2) and (3), which is presented below in terms of fluidic

pressure P:

$$P(L,T)=NP|_{X=X_{\text{end}}}-F_{\text{ext}}$$

$$+\begin{cases}K_{\text{closed}}\left(L-L^c\right)\\F_{\text{open}}^{\text{snap}}+K_s\left(L-L_{\text{open}}^{\text{snap}}\right)\\K_{\text{open}}\left(L-L^o\right)\end{cases}, \quad \begin{matrix}L<L_{\text{open}}^{\text{snap}}\\L_{\text{open}}^{\text{snap}}<L<L_{\text{close}}^{\text{snap}}\\L_{\text{close}}^{\text{snap}}<L,\end{matrix}$$

$$\tag{11b}$$

where

$$F_{\text{open}}^{\text{snap}}=\frac{f_{\text{open}}^{\text{snap}}}{p_c\pi r_c^2}, \quad K_{\text{closed}}=\frac{k_{\text{closed}}l_c}{p_c\pi r_c^2}. \tag{11c}$$

In addition, K_s and K_{open} are normalized identically to K_{closed}, whereas $L_{\text{open}}^{\text{snap}}$, $L_{\text{close}}^{\text{snap}}$, L^c and L^o are normalized by l_c. Note that according to our definition $N=1$ or $N=0$ for the open or closed end, respectively, at $X=X_{\text{end}}$. Moreover, F_{ext} denotes the external force acting on the free end of the straw, in the X-direction.

In order to solve the governing Eq. (11), it is necessary to calculate the transition between different phases. Although this greatly complicates the analysis, in some cases, additional simplifications can be made as is explained in the next sections.

B. A single element in the spinodal

We examine here the case in which only the nth bistable element is in the spinodal region [see Fig. 2(a)]. We require that the rigidity of the open or close phases is much greater than the spinodal, which simplifies the governing equation for the length of a bistable element in each of the different phases to $L_n\approx L^c$ for the open phase, $L_n\approx L^o$ for the close phase, and $L_n\approx L_{\text{open}}^{\text{snap}}+(P-NP|_{X=X_{\text{end}}}+F_{\text{ext}}-F_{\text{open}}^{\text{snap}})/K_s$ for the unstable spinodal phase.

Since the nth element is the only element in the spinodal, $U_b\approx 0$ for all other elements, and Eq. (5) can be directly integrated over X from the inlet to the center of the nth element, yielding

$$P(X,T)|_{X=X_n}=P|_{X=0}-\frac{8}{\pi}X_nQ(T), \tag{12}$$

where X_n is the location of the center of the element at the spinodal phase.

From mass conservation we can set $Q(T)=\pi\varepsilon\partial L_n/\partial T$, yielding the following differential equation for the length of the element in the spinodal, L_n:

$$(L_n-L_{\text{open}}^{\text{snap}})K_s+NP|_{X=X_{\text{end}}}-F_{\text{ext}}+F_{\text{open}}^{\text{snap}}$$

$$=P|_{X=0}-8\varepsilon X_n\frac{\partial L_n}{\partial T}. \tag{13}$$

This equation is supplemented by initial conditions describing the state of the nth element at, say, $T=0$. For
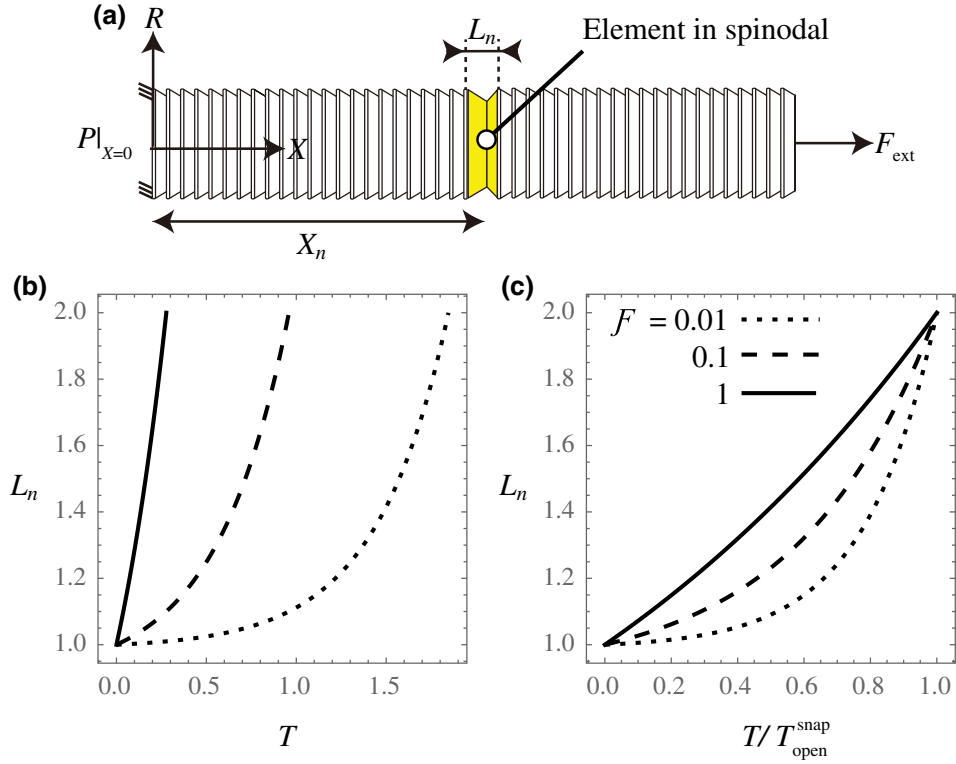
FIG. 2. (a) Schematic illustration of the configuration where only the nth element is in the spinodal. (b) Displacement, L_n, versus time, T, for various values of $\mathcal{F} := F_{\text{ext}} + P|_{X=0} - F_{\text{open}}^{\text{snap}} - NP|_{X=X_{\text{end}}}$, showing that as $\mathcal{F}$ decreases, the nth element is in the spinodal for longer time. (c) Displacement, L_n, versus the scaled time, $T/T_{\text{open}}^{\text{snap}}$, showing that the nonlinearity becomes more evident as $\mathcal{F}$ decreases. The parameters used are $X_n = 1$, $L_{\text{close}}^{\text{snap}} = L^o = 2$, $L_{\text{open}}^{\text{snap}} = L^c = 1$, $\varepsilon = 0.05$, and $\mathcal{F} \in \{0.01, 0.1, 1\}$.

an element which is snapping open from a closed state, the initial condition is $L_n(0) = L_{\text{open}}^{\text{snap}}$, yielding under the simplifying assumption that the inlet and the outlet pressures, namely $P|_{X=0}$ and $P|_{X=X_{\text{end}}}$, are independent of the time, T, that for $0 \leq T \leq T_{\text{open}}^{\text{snap}}$,

$$L_n - L_{\text{open}}^{\text{snap}} = \frac{\mathcal{F}}{K_s}\left(1 - e^{-\frac{K_s T}{8\varepsilon X_n}}\right), \quad (14)$$

where for brevity we use the notation $\mathcal{F} := F_{\text{ext}} + P|_{X=0} - F_{\text{open}}^{\text{snap}} - NP|_{X=X_{\text{end}}}$. The total time in the spinodal phase can be calculated by requiring $L_n \to L^o$ and isolating T, which yields that

$$T_{\text{open}}^{\text{snap}} = \frac{8\varepsilon X_n}{K_s} \log\left[\frac{\mathcal{F}}{\mathcal{F} - K_s(L^o - L_{\text{open}}^{\text{snap}})}\right]. \quad (15)$$

For the case of snapping closed, the initial condition is $L_n(0) = L_{\text{close}}^{\text{snap}}$ and similar calculation yields the time $T_{\text{close}}^{\text{snap}}$. For more details, see Appendix B.

Figure 2 shows the displacement, L_n, during the opening of a single frustum versus T [panel (b)] and versus the rescaled time, $T/T_{\text{open}}^{\text{snap}}$ [panel (c)]. Due to the negative stiffness of the spinodal phase, the fluid pressure at the frusta decreases during the opening process, and thus the rate of

opening of the frusta increases with time. Moreover, as can be seen in Figs. 2(b) and 2(c), as the inlet pressure $P|_{X=0}$ increases and reaches some critical value (depending on the physical parameters of the problem), it succeeds in overcoming the contraction of the straw caused by the elasticity of its walls, so that the fluid flow becomes only slightly affected by the elastic boundaries of the straw. In other words, when the inlet pressure increases, the effect of the spinodal, which is responsible for the nonlinearity in the front propagation, decreases, and the rate of opening of the frusta becomes constant.

C. Sequenced snapping of the bistable elements

Considering bistable elements connected in series and actuated by inlet pressure, the minimal-energy principle requires that the element nearest to the inlet will first switch between phases (since the viscous resistance to the closest element is minimal). Since the spinodal involves negative stiffness, the element in the spinodal will reduce the pressure near it during the snap, and thus further prevent other elements from reaching the spinodal state. After the closest element has finished the snap process, the next closest element will be snapped open, and so forth (see Fig. 3). In this section we will describe this process.
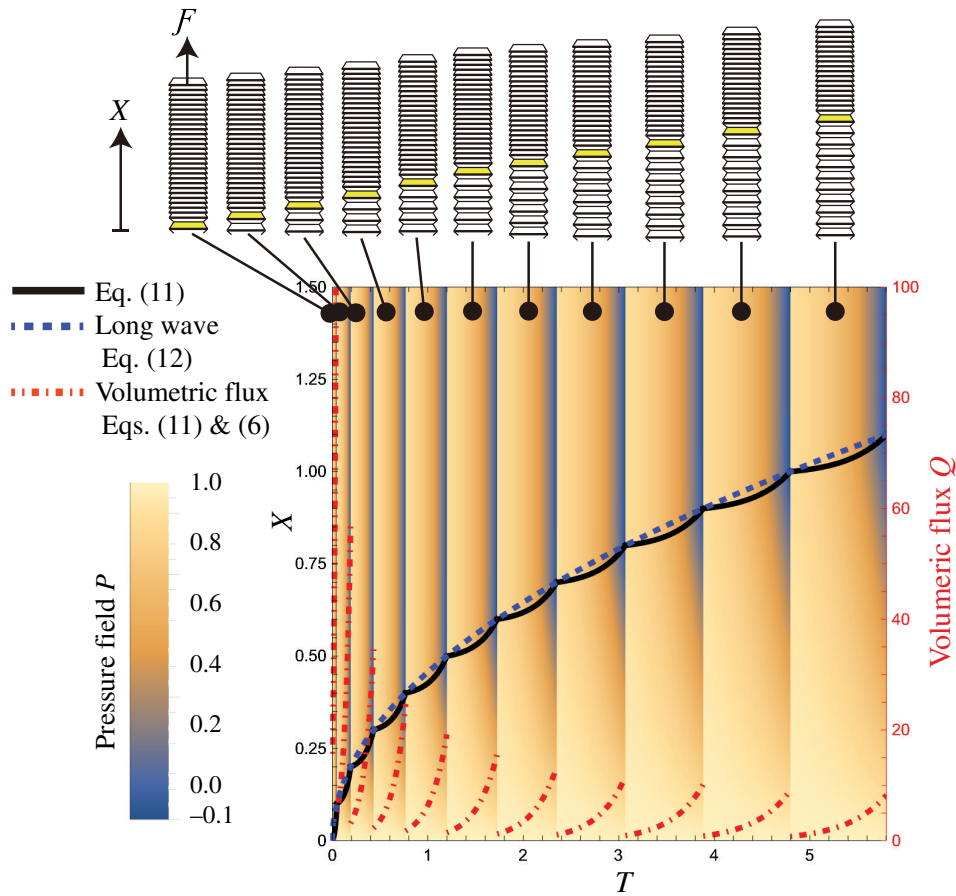
FIG. 3.   Length of the open phase, X_n, calculated according to Eq. (17) (black line) and according to the long-wave approximation in Eq. (18) (blue dashed line) versus time, T. The volumetric flux, Q (dashed red curves), versus time, T, corresponds to the right "Volumetric flux" axis. These curves are overlaid on a colormap representing the pressure field within the straw, where dark and light colors stand for low and high liquid pressure values, respectively. The parameters used are $L_{\text{close}}^{\text{snap}} = L^o = 2$, $L_{\text{open}}^{\text{snap}} = L^c = 1$, $\varepsilon = 0.05$, $K_s = -1$, $P|_{X=0} = 1$, $NP|_{X_{\text{end}}} = 0$, $F_{\text{open}}^{\text{snap}} = 2$, and $F_{\text{ext}} = 1.1$.

First, note that, by definition, the location to the center of the element in the spinodal is given by $X_n = \varepsilon \left(\sum_{m=1}^{n-1} L_m + L_n/2 \right)$. Since all elements before the nth element, namely for $m < n$, have already snapped to the open phase, using Eq. (14), we can set $L_m = L^o$ for the case of initially closed elements (or $L_m = L^c$ for the initially open case).

Thus, the total time needed for the sequenced snapping of n elements can be calculated by summing the snap open times, $T_{\text{open}}^{\text{snap}}$, of all prior elements calculated according to Eq. (15), and using the formula for the sum of arithmetic progression with the first element $X_1 = \varepsilon L^o/2$ and the last element $X_n = \varepsilon n L^o$, leading to

$$\sum_{m=1}^{n} T_m^{\text{snap}} = \frac{4n^2 L^o \varepsilon^2}{K_s} \log \left[\frac{\mathcal{F}}{\mathcal{F} - K_s(L^o - L_{\text{open}}^{\text{snap}})} \right]. \quad (16)$$

In order to find the elongation of the straw, which can be related to the front location, we substitute the expression for L_n given in Eq. (14) into the definition

of X_n, and use that $L_m = L^o$ for all $m < n$ and that the time needed for the opening of the nth element in the sequence (starting from the time at which all previous elements are already snapped open) is $T - \sum_{m=1}^{n-1} T_m^{\text{snap}}$. Moreover, assuming that $L_n/2 \ll \sum_{m=1}^{n-1} L_m$, we get for $\sum_{m=1}^{n-1} T_m^{\text{snap}} \leq T \leq \sum_{m=1}^{n} T_m^{\text{snap}}$ the following explicit expression for X_n:

$$X_n = \varepsilon \left\{ L^o(n-1) + \frac{L_{\text{open}}^{\text{snap}}}{2} + \frac{\mathcal{F}}{2K_s} \left(1 - \tilde{\mathbf{e}} \right) \right\}, \quad (17)$$

where for brevity we use the notation $\tilde{\mathbf{e}} := e^{-\frac{K_s(T - \sum_{m=1}^{n-1} T_m^{\text{snap}})}{8\varepsilon \sum_{m=1}^{n-1} L_m}}$.

Now, $Q(T)$ may be estimated by using that $Q(T) = \pi \varepsilon \partial L_n / \partial T$ and $P(X, T)$ can be calculated according to Eq. (12). On the other hand, the location of the snapping front can also be estimated from a long-wave approximation, thus losing some detail but gaining a simpler description. More specifically, using Eq. (15) and
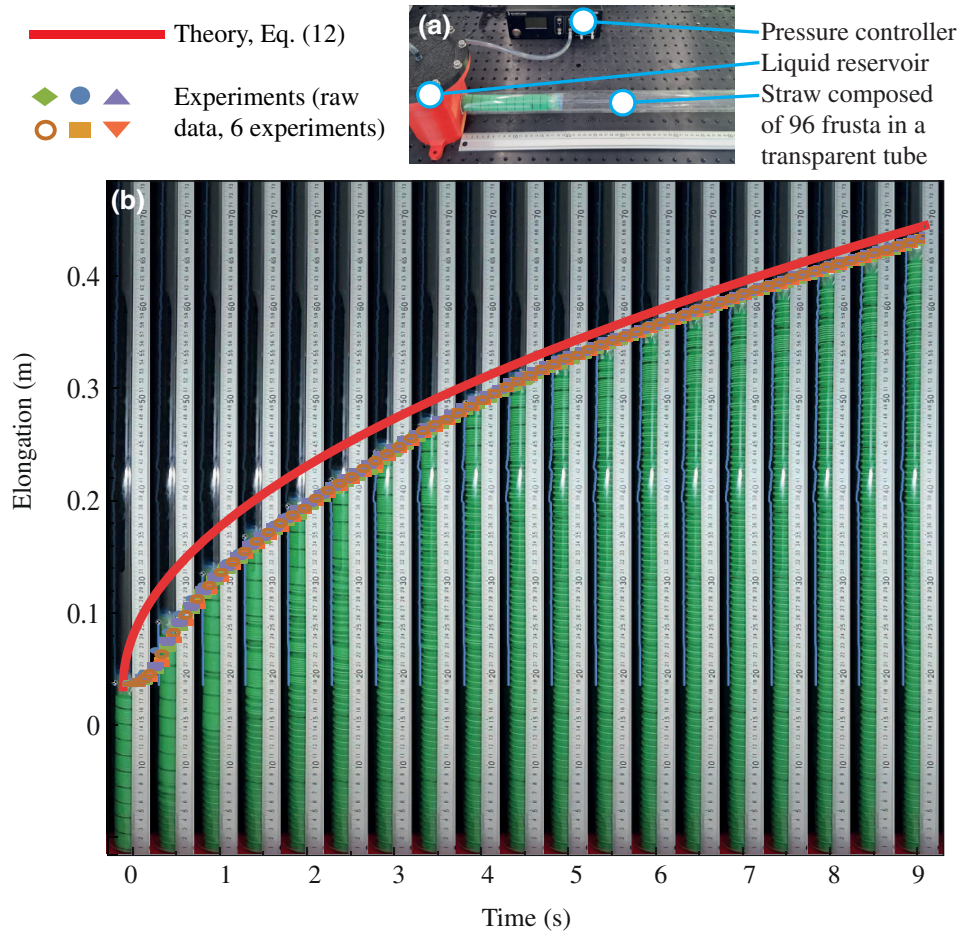
FIG. 4. (a) The experimental setup, consisting of a gas pressure controller, a liquid container, and a straw with 96 frusta connected in series. (b) A comparison between the model (red curve denotes the long-wave approximation) and the experimental data (colorful marks denote raw data from six experiments). These results are overlaid on a sequence of frames from a single experiment movie for the different times. An excellent agreement between the experiment and the model was achieved without any fitting parameters, where all data regarding the geometric and physical properties of the frusta were taken from an earlier paper [60]. A video comparing theory to experiment is available in the Supplementary Material [59].

averaging over the snaps, we get that

$$\frac{\partial X_n}{\partial T} = \frac{\varepsilon L^o}{T_{\text{open}}^{\text{snap}}} = \frac{L^o K_s}{8 X_n} \left\{ \log\left[\frac{\mathcal{F}}{\mathcal{F} - K_s(L^o - L_{\text{open}}^{\text{snap}})} \right] \right\}^{-1}.$$

Solving this equation, we obtain that the position of the front is given by

$$X_n = \sqrt{\frac{L^o K_s T}{4} \left\{ \log\left[\frac{\mathcal{F}}{\mathcal{F} - K_s(L^o - L_{\text{open}}^{\text{snap}})} \right] \right\}^{-1}}. \quad (18)$$

In Fig. 3 we show the length of the opened phase which was calculated according to Eq. (17) (black solid curve corresponding to the left X coordinate axis), the length of the opened phase which was calculated according to the long-wave approximation in Eq. (18) (blue dashed curve corresponding to the left X coordinate axis), and the volumetric

flux, Q, which was calculated as mentioned above (dashed red curves corresponding to the right "Volumetric flux" axis) versus time, T. Note that the elongation of the straw is $X_n(L^o - L_{\text{open}}^{\text{snap}})/L^o$. The colors in the figure represent the corresponding pressure field within the straw, where the pressure was calculated according to Eq. (12). It can be seen that as the number of snapped open frusta increases, the duration of each phase increases as well, that is, it takes more and more time between the following snaps. Furthermore, since the volume per opening of each frusta is identical, the flux within the straw becomes slower, where the slowdown of the flux is inversely proportional to the increase of viscous resistance.

Moreover, it is evident from Fig. 3 that there exist two time scales in the system: one short time scale which is the characteristic time taken got one element to snap open, and a second, longer time scale, which is the characteristic time taken for the whole structure to open. At the short time
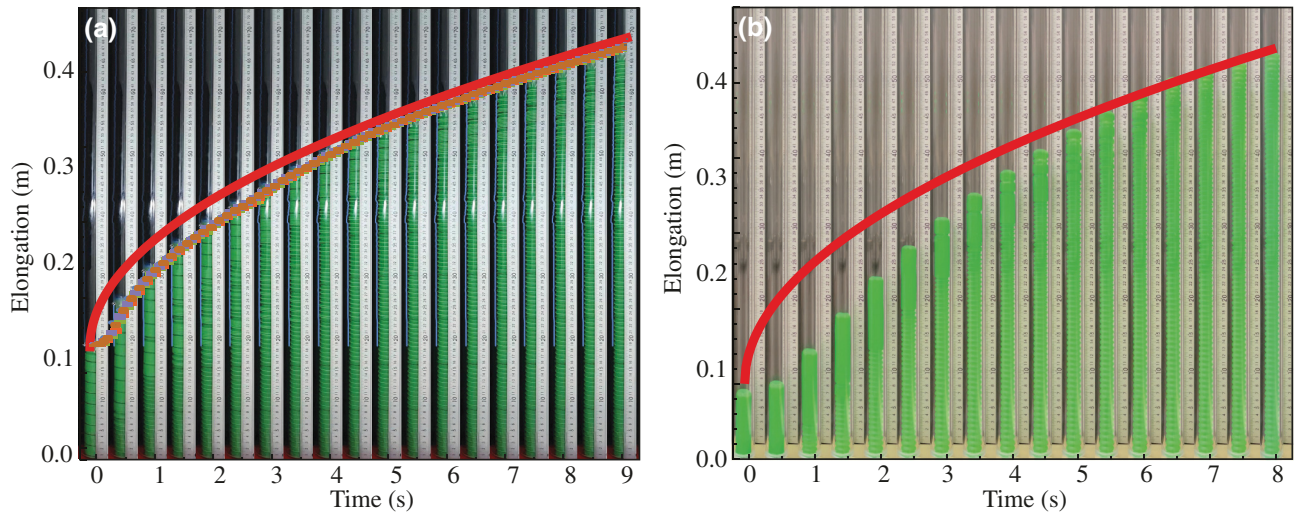
FIG. 5. A comparison between the model (red curve denotes the long-wave approximation) and the experimental data in two cases of parameters: (a) the straw is with 96 frusta and the rest of parameters are as given in Eqs. (C1) (this is the same as Fig. 4) and (b) the straw is with 78 frusta and the rest of parameters are as given in Eqs. (C2). These results are overlaid on a sequence of frames from corresponding experiment movies for the different times. Excellent agreement between the experiment and the model was achieved without any fitting parameters. A video comparing theory to experiment is available in the Supplementary Material [59].

scale the gradients in the pressure, flux, and the position of the front are much larger than at the long time scale. Note that the long-wave approximation coincides with the full solution at the times where snapping open occurs, but it does not catch well the front position at intermediate times, between the snaps. Thus, it approximates well the behavior of the front propagation at the long time scale but misses the details occurring at the short time scale.

Figure 4 compares the experimental results and the long-wave model. There is a small initial discrepancy between experimental and theoretical results, which diminishes in time, so that overall there is excellent agreement. The parameters used in the calculation were not fitted to the experiment, but rather were taken as is from a different paper which used exactly the same straws [60]. As expected by theory, in the experimental results there is a sequenced (ordered) opening of the frusta, starting from the inlet and propagating towards the outlet. In some instances, however, several frusta may open before their turn, which may be the result of manufacturing defects. Additional examples are presented in Appendices C and D, which includes experimental data for different straw parameters and different internal fluids, as well as data on impact mitigation experiments.

IV. CONCLUDING REMARKS

Motivated by a desire to revolutionize applications such as foldable structures, vibration mitigation, shock attenuation, soft robotics, reconfigurable materials, and more, multistable metamaterials have been extensively studied in recent years and new multistable materials with unique behaviors have been developed. The reason for the interest in multistable metamaterials lies in their inherent ability to provide large reversible deformations, mechanical memory, and structural programmability. Nevertheless, existing works have focused on tailoring the structural properties of the unit cells to obtain desired multistable behavior, while the rate-related properties have largely been overlooked. This disconnect between the above-mentioned vision and the current realization of multistable metamaterial is the main motivation for this work.

In this study we examined the concept of incorporating internal flows inside multistable metamaterials. Using strawlike structures as a simple prototypical model, we studied the two-way interaction between internal viscous flow and the overall behavior of the multistable structure. A simple analytical model, free of fitting parameters and showing excellent agreement with experiments, has provided important insights regarding this behavior and in particular on the propagation of phase-transition fronts. For example, we were able to obtain explicit relations for controlling the rate and direction of a transition front depending on the relative location of the fluidic inlet. Such ability to tailor both the structural properties as well as the rate-related properties of multistable metamaterials paves the way for the development of new materials that feature large reversible deformations and tailored dynamic properties.

APPENDIX A: FORMULATION OF A FLUID FLOW INSIDE A MULTISTABLE STRAW

Let us consider a viscous, incompressible flow inside a straw, which constitutes a long channel, comprised of many frusta in series, as illustrated in Fig. 1. The

streamwise coordinate, which passes through the center of the channel, and the flow-velocity component are denoted by x and $u = u(x, \mathbf{x}_{cs})$, respectively, while the in-plane cross-section coordinate and the velocity vector are denoted by $\mathbf{x}_{cs}$ and $\mathbf{u}_{cs} = \mathbf{u}_{cs}(x, \mathbf{x}_{cs})$. This notation describes the general case, where the cross section is yet to be defined. Elsewhere in this work we adopt an axisymmetric cylindrical system of coordinates, with longitudinal axis passing through the center of the channel denoted by x and with radial coordinate denoted by $\mathbf{r}$, respectively. This transforms our in-plane coordinate vector to $\mathbf{x}_{cs} = \mathbf{r}$ and the in-plane flow velocity to $\mathbf{u}_{cs} = \mathbf{u}_{cs}(x, \mathbf{r})$. In addition, in what follows, the operator ∇_{cs} represents in-plane spatial gradient inside the cross section, p is the relative (gauge) pressure of the fluid, with μ and ρ denoting its material properties, representing dynamic viscosity and density, respectively. Henceforth, all lower-case letters represent dimensional quantities, upper-case letters represent normalized dimensionless quantities, and superscript asterisks $(\,)^*$ denote characteristic quantities (e.g., $x = x^* X$).

Using this notation, we may express the momentum and continuity equations as

$$\rho \left(\frac{\partial u}{\partial t} + u \frac{\partial u}{\partial x} + \mathbf{u}_{cs} \cdot \nabla_{cs} u \right) = \mu \left(\frac{\partial^2 u}{\partial x^2} + \nabla_{cs}^2 u \right) - \frac{\partial p}{\partial x},$$
(A1)

$$\rho \left(\frac{\partial \mathbf{u}_{cs}}{\partial t} + u \frac{\partial \mathbf{u}_{cs}}{\partial x} + \mathbf{u}_{cs} \cdot \nabla_{cs} \mathbf{u}_{cs} \right)$$
$$= \mu \left(\frac{\partial^2 \mathbf{u}_{cs}}{\partial x^2} + \nabla_{cs}^2 \mathbf{u}_{cs} \right) - \nabla_{cs} p,$$
(A2)

$$\nabla_{cs} \cdot \mathbf{u}_{cs} + \frac{\partial u}{\partial x} = 0.$$
(A3)

As we consider an axisymmetric configuration, we introduce the base radius of the straw (excluding the frusta), and denote it by r_c. Note that r_c is constant along the axis of the straw, x. We assume a viscous (i.e., with small Reynolds number, Re $\ll 1$), Newtonian, and incompressible flow that mostly occurs through the bulk area of the straw, and neglect possible flow or turbulence in the vicinity of the boundary, setting no-slip and no-penetration boundary conditions there. Furthermore, we assume that the velocity of the boundary in the longitudinal direction resulting from the snap of a frustum, which we denote by u_b, is axisymmetric as well, namely $u_b = u_b(x)$. Finally, we employ the lubrication assumption, which in our case means that $x_{cs}^* \ll x^*$ and $u_{cs}^* \ll u^*$.

Following dimensional analysis, similarly to what we have shown in the appendix of our previous work [61],

these assumptions reduce Eqs. (A1) and (A2) to

$$\nabla_{cs}^2 u = \frac{1}{\mu} \frac{\partial p}{\partial x},$$
(A4)

$$\nabla_{cs} p = 0,$$
(A5)

and Eq. (A5) yields that $p = p(x)$. Next, we integrate Eq. (A3) across the cross-sectional plane (with respect to coordinates $\mathbf{x}_{cs}$), employ Gauss's theorem and the Reynolds transport theorem together with no-penetration conditions, and obtain that

$$\frac{\partial q}{\partial x} = 0,$$
(A6)

where q is the fluid flux through the cross section, defined as

$$q = \int_{cs} u(x, \mathbf{x}_{cs}) \, d\mathbf{x}_{cs}.$$
(A7)

We solve Eq. (A4), which is a general Poisson equation in the cross-sectional plane (since p is independent of $\mathbf{x}_{cs}$). In our case, due to the axial symmetry, it is reduced to a second-order ordinary differential equation (ODE) with respect to r. We use no-slip boundary conditions, namely that $u(x, r_c) = u_b(x)$, where u_b is the speed of the walls in the x-direction, and obtain that

$$u(x, r) = \frac{1}{4\mu} \frac{\partial p(x)}{\partial x} (r^2 - r_c^2) + u_b(x).$$
(A8)

Integral mass conservation and the no-penetration condition at $r = r_c$ yield

$$\frac{\partial}{\partial x} \int_0^{r_c} u_x r \, dr = 0.$$
(A9)

Substituting the solution for u in Eq. (A8) into Eq. (A7), we obtain that

$$q = \pi r_c^2 u_b - \frac{\pi r_c^4}{8\mu} \frac{\partial p}{\partial x},$$
(A10)

which yields the following second-order ODE for $p(x)$:

$$\frac{\partial}{\partial x} \left(u_b - \frac{r_c^2}{8\mu} \frac{\partial p}{\partial x} \right) = 0.$$
(A11)

Note that Eq. (A11) governs the flow balance in an arbitrary infinitesimal section inside the straw. We use this equation to analyze finite sections of the straw, in order to gain insight into the dynamical behavior of the system during the snapping.

Transforming Eq. (A8) into dimensionless variables yields the characteristic velocity $u_c = p_c r_c^2/\mu x_c$, and the normalized equation is given by

$$U(X, T) = U_b(X, T) + \frac{\partial P}{\partial X} \frac{R^2 - 1}{4}. \tag{A12}$$

APPENDIX B: CALCULATION OF SNAP CLOSE TIME FOR A SINGLE ELEMENT IN SPINODAL

For the case of snapping close, instead of Eq. (14), we get that

$$L_n - L_{\text{close}}^{\text{snap}} e^{-\frac{K_S T}{8\varepsilon X_n}} = \left(L_{\text{open}}^{\text{snap}} + \frac{\mathcal{F}}{K_s} \right) \left(1 - e^{-\frac{K_S T}{8\varepsilon X_n}} \right), \tag{B1}$$

which yields, subject to the initial condition $L_n(0) = L_{\text{close}}^{\text{snap}}$, that

$$T_{\text{close}}^{\text{snap}} = \frac{8\varepsilon X_n}{K_s} \log \left[\frac{\mathcal{F} - K_s(L_{\text{close}}^{\text{snap}} - L_{\text{open}}^{\text{snap}})}{\mathcal{F} - K_s(L^c - L_{\text{open}}^{\text{snap}})} \right]. \tag{B2}$$

APPENDIX C: VALIDATING OUR THEORETICAL RESULTS AGAINST EXPERIMENT

1. Experimental procedure

The findings in the paper were experimentally validated utilizing the demonstrator presented in Fig. 4(a). The demonstrator setup consists of a 3D printed reservoir filled with silicone oil. The pressure in the reservoir is governed by an Elveflow OB1 Mk3 piezoelectric pressure controller. An off-the-shelf polymer straw is glued horizontally to the reservoir as a cantilever and sealed at its far end. The straw is inserted into a rigid transparent tube constraining the motion to be one-dimensional. The parameters that we used in Figs. 4 and 5(a) are as follows:

$$\mu = 60\,\text{Pa s}, \quad r_o = 14.65 \times 10^{-3}\,\text{m}, \quad r_c = 11 \times 10^{-3}\,\text{m},$$
$$l^o = 5.98 \times 10^{-3}\,\text{m}, \quad l^c = 1.72 \times 10^{-3}\,\text{m},$$
$$k_s = -6226\,\text{Pa m}, \quad p|_{x=0} = 90 \times 10^3\,\text{Pa},$$
$$f_{\text{snap}}^{\text{open}} = 17.085\,\text{Pa m}^2, \quad f_{\text{ext}} = 0, \quad N = 0. \tag{C1}$$

The experiment shown in the paper was repeated six times: the inflating experiment was started when the system was in rest at pressure of 100 mbar (the snap open pressure of each frustum was found experimentally to be approximately 262 mbar). Then, the pressure was set to 900 mbar and the straw movement was captured by video until it reached its new equilibrium. The experiments were captured on video in 1080p resolution and at 30 frames per second. Using Kinovea software, each video was analyzed by tracking the tip location of the straw and finally obtaining the tip location as a function of time. See the video in the Supplementary Material comparing theory to experiment [59].

Moreover, in order to visualize that our model validity is independent of the parameters of the straw and the applied inlet pressure, we present here an additional example of an experiment with silicone oil, whose parameters are as follows:

$$\mu = 60\,\text{Pa s}, \quad r_o = 9.5 \times 10^{-3}\,\text{m}, \quad r_c = 6.5 \times 10^{-3}\,\text{m},$$
$$l^o = 4.82 \times 10^{-3}\,\text{m}, \quad l^c = 1.38 \times 10^{-3}\,\text{m},$$
$$k_s = -3119\,\text{Pa m}, \quad p|_{x=0} = 200 \times 10^3\,\text{Pa},$$
$$f_{\text{snap}}^{\text{open}} = 6.24\,\text{Pa m}^2, \quad f_{\text{ext}} = 0, \quad N = 0. \tag{C2}$$

Note that, as expected by theory, in the experiments there is a sequenced (ordered) opening of the frusta, starting from the inlet and propagating towards the outlet. In some instances, however, several frusta may open before their turn, which may be the result of manufacturing defects. Moreover, note that in the theoretical simulation in the case of the parameters in Eqs. (C1) we used 108 frusta since the total length of the open straw in this case was approximately 0.65 m and the length of the frusta in the open phase was $l^o = 5.98 \times 10^{-3}\,\text{m}$, which results in $n = \lfloor 0.65/(5.98 \times 10^{-3}) \rfloor = 108$.

Furthermore, in order to demonstrate the importance of the requirement of the fluid viscosity, we conducted two additional experiments with inviscid fluids: water and air
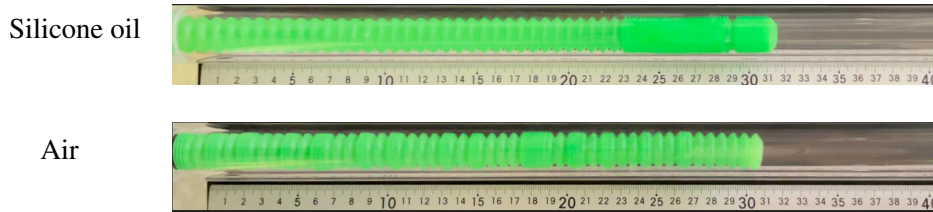

FIG. 6. A comparison of the straw phase distributions in two cases of internal fluid: silicone oil with a viscosity of 60 Pa s and air with negligible viscosity.
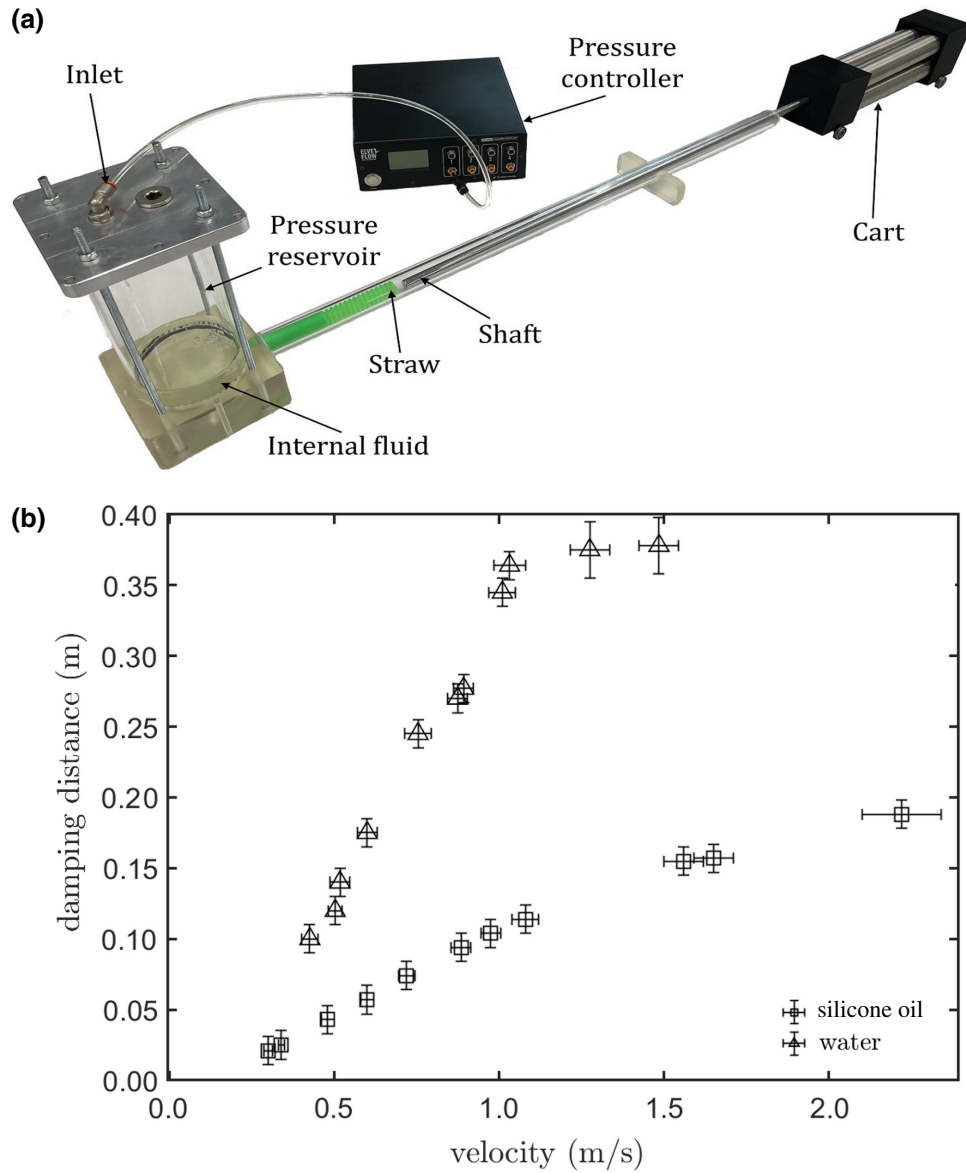
FIG. 7. (a) The setup for damping experiments, consisting of a cart and a shaft which collide with a multistable straw filled with a fluid and connected to a pressure reservoir and a pressure controller. (b) The experimental results extracted from the collisions of the cart (with a shaft) with the straw, showing the damping distance of the straw, that is, the maximal distance that it shortens as a result of the collision, versus the shaft velocity with two different internal fluids: water and silicone oil with a viscosity of 60 Pa s.

with the following sets of parameters:

$$\mu = 10^{-3} \, \text{Pa s}, \quad r_o = 9.5 \times 10^{-3} \, \text{m}, \quad r_c = 6.5 \times 10^{-3} \, \text{m},$$

$$l^o = 4.82 \times 10^{-3} \, \text{m}, \quad l^c = 1.38 \times 10^{-3} \, \text{m},$$

$$k_s = -3119 \, \text{Pa m}, \quad p|_{x=0} = 45 \times 10^3 \, \text{Pa}$$

$$f_{\text{snap}}^{\text{open}} = 6.24 \, \text{Pa m}^2, \quad f_{\text{ext}} = 0, \quad N = 0 \tag{C3}$$

and

$$\mu = 1.81 \times 10^{-5} \, \text{Pa s}, \quad r_o = 9.5 \times 10^{-3} \, \text{m},$$

$$r_c = 6.5 \times 10^{-3} \, \text{m}, \quad l^o = 4.82 \times 10^{-3} \, \text{m},$$

$$l^c = 1.38 \times 10^{-3} \, \text{m}, \quad k_s = -3119 \, \text{Pa m}, \tag{C4}$$

$$p|_{x=0} = 45 \times 10^3 \, \text{Pa}, \quad f_{\text{snap}}^{\text{open}} = 6.24 \, \text{Pa m}^2,$$

$$f_{\text{ext}} = 0, \quad N = 0,$$

respectively. Figure 6 shows an example of straw elongation filled with either silicone oil or air. It can be seen that viscous internal fluid (silicone oil) results in an approximately sequenced straw elongation, whereas an inviscid fluid (air) results in a random order of frusta opening.

For a video showing a comparison between the straw dynamics in the three cases—viscous oil with the

parameters in (C2), water, and air—see the video in the Supplementary Material [59]. Also in the video, it can be observed that in the case of inviscid fluid the elongation dynamics is completely different relative to the case with viscous flow, and in particular when using inviscid fluid there is no sequenced ordering in the opening of the frusta, but the order of the opening is random.

2. Converting our results to dimensional form

Equation (14), converted into dimensional form, is given by

$$
l_n(t) - l_{\text{open}}^{\text{snap}} = \left[\frac{f_{\text{open}}^{\text{snap}} - f_{\text{ext}} + \pi r_c^2 \left(Np|_{x=x_{\text{end}}} - p|_{x=0} \right)}{k_s} \right]
$$
$$
\times \left(e^{-\frac{k_s t}{8\pi \mu x_n}} - 1 \right), \tag{C5}
$$

where x_n is the location of the frustum currently in the spinodal phase (opening or closing) and t is time so that $t = 0$ corresponds to the moment at which this frustum switched to the spinodal phase. The elongation of frustum n is calculated according to $l_n(l^o - l_{\text{open}}^{\text{snap}})/l^o$. For the case of sequenced opening of the frustum, the value of the function x_n can be estimated by Eq. (17), which, transformed to dimensional variables, is given for $\sum_{m=1}^{n-1} t_m^{\text{snap}} \leq t \leq \sum_{m=1}^{n} t_m^{\text{snap}}$ by

$$
x_n = l^o(n - 1) + 0.5 l_{\text{open}}^{\text{snap}}
$$
$$
+ g \times \left(e^{-\frac{k_s(t - \sum_{m=1}^{n-1} t_m^{\text{snap}})}{8\pi \mu \sum_{m=1}^{n-1} l_m}} - 1 \right), \tag{C6}
$$

where according to Eq. (16) the sum of dimensional snap open times is given by

$$
\sum_{m=1}^{n} t_m^{\text{snap}} = \frac{4\pi \mu n^2 l^o}{k_s} \log \left[\frac{g}{g + k_s(l^o - l_{\text{open}}^{\text{snap}})} \right]. \tag{C7}
$$

In Eqs. (C6) and (C7), for brevity we use g which is defined as

$$
g = f_{\text{open}}^{\text{snap}} - f_{\text{ext}} + \pi r_c^2 \left(Np|_{x=x_{\text{end}}} - p|_{x=0} \right).
$$

Furthermore, the long-wave approximation, which is given in Eq. (18), may be expressed in dimensional form as

$$
x_n(t) = \sqrt{\frac{l^o k_s t}{4\pi \mu} \left\{ \log \left[\frac{g}{g + k_s(l^o - l_{\text{open}}^{\text{snap}})} \right] \right\}^{-1}}. \tag{C8}
$$

Note that the elongation of the straw is calculated according to $x_n(l^o - l_{\text{open}}^{\text{snap}})/l^o$.

APPENDIX D: IMPACT MITIGATION TUNING

One possible application for the incorporation of viscous fluids in multistable structures is to tune impact mitigation. To visualize the capability of our concept for damping, we have constructed an experimental setup, shown in Fig. 7(a). In our experiments, a cart collided at different velocities with a multistable straw filled with either silicone oil or water, and the damping distance (the maximal distance that the straw shortens in response to the collision) was calculated as a function of the cart velocity. The results of our experiments are shown in Fig. 7(b). It can be clearly seen that the damping distances in experiments with silicone oil are much smaller than the corresponding distances in the experiments with water. Moreover, the difference between the distances in the two types of experiments is enhanced by increasing the velocity of the cart. Hence, since the effectiveness of the damping is reflected by the magnitude of the damping distance (as the damping distance decreases the damping is more efficient), we can conclude that silicone oil leads to a much more efficient damping than water, and this is especially evident at high velocities.

[1] G. Librandi, E. Tubaldi, and K. Bertoldi, Programming nonreciprocity and reversibility in multistable mechanical metamaterials, Nat. Commun. **12**, 3454 (2021).

[2] O. R. Bilal, A. Foehr, and C. Daraio, Bistable metamaterial for switching and cascading elastic vibrations, Proc. Natl. Acad. Sci. U.S.A. **14**, 4603 (2017).

[3] V. Ramakrishnan and M. J. Frazier, Multistable metamaterial on elastic foundation enables tunable morphology for elastic wave control, J. Appl. Phys. **127**, 225104 (2020).

[4] H. Yang and L. Ma, Multi-stable mechanical metamaterials with shape-reconfiguration and zero Poisson's ratio, Mater. Des. **152**, 181 (2018).

[5] I. Benichou and S. Givli, Force-sensitive metamaterials for vibration mitigation and mechanical protection, Extreme Mech. Lett. **40**, 100932 (2020).

[6] M. F. Berwind, A. Kamas, and C. Eberl, A hierarchical programmable mechanical metamaterial unit cell showing metastable shape memory, Adv. Eng. Mater. **20**, 1800771 (2018).

[7] Z. Meng, M. Liu, Y. Zhang, and C. Q. Chen, Multistep deformation mechanical metamaterials, J. Mech. Phys. Solids **144**, 104095 (2020).

[8] F. Pan, Y. Li, Z. Li, J. Yang, B. Liu, and Y. Chen, 3D pixel mechanical metamaterials, Adv. Mater. **31**, 1900548 (2019).

[9] B. Haghpanah, L. Salari-Sharif, P. Pourrajab, J. Hopkins, and L. Valdevit, Multistable shape-reconfigurable architected materials, Adv. Mater. **28**, 7915 (2016).

[10] O. Peretz, A. K. Mishra, R. F. Shepherd, and A. D. Gat, Underactuated fluidic control of a continuous multistable membrane, Proc. Natl. Acad. Sci. U.S.A. **117**, 5217 (2020).

[11] E. Ben-Haim, L. Salem, Y. Or, and A. D. Gat, Single-input control of multiple fluid-driven elastic actuators via

interaction between bistability and viscosity, Soft Robot. **7,** 259 (2020).

[12] S. Babaee, J. Shim, J. C. Weaver, E. R. Chen, N. Patel, and K. Bertoldi, 3D soft metamaterials with negative Poisson's ratio, Rapid Prototyp. J. **25,** 5044 (2013).

[13] J. J. do Rosário, J. B. Berger, E. T. Lilleodden, R. M. McMeeking, and G. A. Schneider, The stiffness and strength of metamaterials based on the inverse opal architecture, Extreme Mech. Lett. **12,** 86 (2017).

[14] X. Zheng, H. Lee, T. H. Weisgraber, M. Shusteff, J. DeOtte, E. B. Duoss, J. D. Kuntz, M. M. Biener, Q. Ge, J. A. Jackson, S. O. Kucheyev, N. X. Fang, and C. M. Spadaccin, Ultralight, ultrastiff mechanical metamaterials, Science **344,** 1373 (2014).

[15] K. Bhattacharya and R. D. James, The material is the machine, Science **307,** 53 (2005).

[16] E. Faran and D. Shilo, The kinetic relation for twin wall motion in NiMnGa, J. Mech. Phys. Solids **59,** 975 (2011).

[17] R. Khajehtourian and D. M. Kochmann, Phase transformations in substrate-free dissipative multistable metamaterials, Extreme Mech. Lett. **37,** 100700 (2020).

[18] S. Katz and S. Givli, Solitary waves in a bistable lattice, Extreme Mech. Lett. **22,** 106 (2018).

[19] S. Katz and S. Givli, Boomerons in a 1-D lattice with only nearest-neighbor interactions, EPL **131,** 64002 (2020).

[20] C. Gao, V. Slesarenko, M. C. Boyce, S. Rudykh, and Y. Li, Instability-induced pattern transformation in soft metamaterial with hexagonal networks for tunable wave propagation, Sci. Rep. **8,** 11834 (2018).

[21] A. G. Izard and L. Valdevit, Magnetoelastic metamaterials for energy dissipation and wave filtering, Adv. Eng. Mater. **22,** 1901019 (2020).

[22] Y. Chen and L. Jin, Reusable energy-absorbing architected materials harnessing snapping-back buckling of wide hyperelastic columns, Adv. Funct. Mater. **31,** 2102113 (2021).

[23] S. Nitecki and S. Givli, The mechanical behavior of 2-D lattices with bi-stable springs, J. Mech. Phys. Solids **157,** 104634 (2021).

[24] B. Zhang, Ph.D. thesis, University of Oxford, 2017.

[25] N. P. Bende, T. Yu, N. A. Corbin, M. A. Dias, C. D. Santangelo, J. A. Hanna, and R. C. Hayward, Overcurvature induced multistability of linked conical frusta: how a "bendy straw" holds its shape, Soft Matter **14,** 8636 (2018).

[26] S. Canic and A. Mikelic, Effective equations modeling the flow of a viscous incompressible fluid through a long elastic tube arising in the study of blood flow through small arteries, SIAM J. Appl. Dyn. Syst. **2,** 431 (2003).

[27] L. Manfredi, E. Capoccia, G. Ciuti, and A. Cuschieri, A soft pneumatic inchworm double balloon (SPID) for colonoscopy, Sci. Rep. **9,** 1 (2019).

[28] R. F. Shepherd, F. Ilievski, W. Choi, S. A. Morin, A. A. Stokes, A. D. Mazzeo, X. Chen, M. Wang, and G. M. Whitesides, Multigait soft robot, Proc. Natl. Acad. Sci. U.S.A. **108,** 20400 (2011).

[29] S. A. Morin, R. F. Shepherd, S. W. Kwok, A. A. Stokes, A. Nemiroski, and G. M. Whitesides, Camouflage and display for soft machines, Science **337,** 828 (2012).

[30] R. F. Shepherd, A. A. Stokes, J. Freake, J. Barber, P. W. Snyder, A. D. Mazzeo, L. Cademartiri, S. A. Morin, and

G. M. Whitesides, Using explosions to power a soft robot, Angew. Chem. **52,** 2892 (2013).

[31] A. A. Stokes, R. F. Shepherd, S. A. Morin, F. Ilievski, and G. M. Whitesides, A hybrid combining hard and soft robots, Soft Robot. **1,** 70 (2014).

[32] S. B. Elbaz and A. D. Gat, Dynamics of viscous liquid within a closed elastic cylinder subject to external forces with application to soft robotics, J. Fluid Mech. **758,** 221 (2014).

[33] N. Vasios, A. J. Gross, S. Soifer, J. T. B. Overvelde, and K. Bertoldi, Harnessing viscous flow to simplify the actuation of fluidic soft robots, Soft Robot. **7,** 1 (2020).

[34] P. Polygerinos, N. Correll, S. A. Morin, B. Mosadegh, C. D. Onal, K. Petersen, M. Cianchetti, M. T. Tolley, and R. F. Shepherd, Soft robotics: Review of fluid-driven intrinsically soft devices; manufacturing, sensing, control, and applications in human-robot interaction, Adv. Eng. Mater. **19,** 1700016 (2017).

[35] A. V. Desai, J. D. Tice, C. A. Apblett, and P. J. A. Kenis, Design considerations for electrostatic microvalves with applications in poly (dimethylsiloxane)-based microfluidics, Lab Chip **12,** 1078 (2012).

[36] T. Thorsen, S. J. Maerkl, and S. R. Quake, Microfluidic large-scale integration, Science **298,** 580 (2002).

[37] M. A. Unger, H.-P. Chou, T. Thorsen, A. Scherer, and S. R. Quake, Monolithic microfabricated valves and pumps by multilayer soft lithography, Science **288,** 113 (2000).

[38] T. W. Lowe and T. J. Pedley, Computation of stokes flow in a channel with a collapsible segment, J. Fluids Struct. **9,** 885 (1995).

[39] M. Heil and T. J. Pedley, Large axisymmetric deformation of a cylindrical shell conveying a viscous flow, J. Fluids Struct. **9,** 237 (1995).

[40] M. Heil, The stability of cylindrical shells conveying viscous flow, J. Fluids Struct. **10,** 173 (1996).

[41] M. P. Paidoussis, *Fluid-Structure Interactions: Slender Structures and Axial Flow* (Academic Press, Oxford, 1998), Vol. 1.

[42] S. D. Guest and S. Pellegrino, Analytical models for bistable cylindrical shells, Proc. R. Soc. A: Math. Phys. Eng. Sci. **462,** 839 (2006).

[43] K. Seffen, in *45th AIAA/ASME/ASCE/AHS/ASC Structures, Structural Dynamics & Materials Conference* (American Institute of Aeronautics and Astronautics (AIAA), Palm Springs, California, 2004), p. 1526.

[44] B. Gorissen, D. Melancon, N. Vasios, M. Torbati, and K. Bertoldi, Inflatable soft jumper inspired by shell snapping, Sci. Robot. **5,** eabb1967 (2020).

[45] M. Follador, A. T. Conn, and J. Rossiter, Bistable minimum energy structures (BiMES) for binary robotics, Smart Mater. Struct. **24,** 065037 (2015).

[46] H. Rodrigue, W. Wang, M.-W. Han, T. J. Y. Kim, and S.-H. Ahn, An overview of shape memory alloy-coupled actuators and robots, Soft Robot. **4,** 3 (2017).

[47] B. Treml, A. Gillman, P. Buskohl, and R. Vaia, Origami mechanologic, Proc. Natl. Acad. Sci. U.S.A. **115,** 6916 (2018).

[48] D. Ilssar, M. Pukshansky, Y. Or, and A. D. Gat, Dynamics of Reconfigurable Strawlike Elements, Phys. Rev. Appl. **18,** 034041 (2022).

[49] J. O. Almen and A. Laszlo, The uniform section disc spring, Trans ASME **58**, 305 (1936).

[50] I. Müller and P. Villaggio, A model for an elastic-plastic body, Arch. Ration. Mech. Anal. **65**, 25 (1977).

[51] I. Müller and H. Xu, On the pseudo-elastic hysteresis, Acta Metall. Mater. **39**, 263 (1991).

[52] B. Fedelich and G. Zanzotto, Hysteresis in discrete systems of possibly interacting elements with a double-well energy, J. Nonlinear Sci. **2**, 319 (1992).

[53] T. L. Allinger, M. Epstein, and W. Herzog, Stability of muscle fibers on the descending limb of the force-length relation. A theoretical consideration, J. Biomech. **29**, 627 (1996).

[54] J. A. Shaw and S. Kyriakides, On the nucleation and propagation of phase transformation fronts in a niti alloy, Acta Mater. **45**, 683 (1997).

[55] G. Puglisi and L. Truskinovsky, Mechanics of a discrete chain with bi-stable elements, J. Mech. Phys. Solids **48**, 1 (2000).

[56] A. Luongo, S. Casciati, and D. Zulli, Perturbation method for the dynamic analysis of a bistable oscillator under slow harmonic excitation, Smart Struct. Syst. **18**, 183 (2016).

[57] I. Benichou, E. Faran, D. Shilo, and S. Givli, Application of a bi-stable chain model for the analysis of jerky twin boundary motion in NiMnGa, Appl. Phys. Lett. **102**, 011912 (2013).

[58] T. Cohen and S. Givli, Dynamics of a discrete chain of bistable elements: a biomimetic shock absorbing mechanism, J. Mech. Phys. Solids **64**, 426 (2014).

[59] See Supplemental Material at http://link.aps.org/supplemental/10.1103/PhysRevApplied.18.064077 for a movie containing a comparison between theoretical and experimental results for straw elongation with silicone oil and a comparison between straw dynamics when three different internal fluids are used: water, air, and silicone oil.

[60] O. Peretz, E. B. Abu, A. Zigelman, S. Givli, and A. D. Gat, A metafluid with multistable density and internal energy states, Nat. Commun. **13**, 1810 (2022).

[61] P. Breitman, Y. Matia, and A. D. Gat, Fluid mechanics of pneumatic soft robots, Soft Robot. **8**, 519 (2021).